Journal of Marine Research, 72, 383–403, 2014

On the structure and distribution of thin anticyclonic lenses in the southeast Pacific Ocean

by T. Rossby[1,2]

ABSTRACT

The velocity structure of an anticyclonic lens in the southeast Pacific centered at 300–400 m depth was scanned in detail with a 75 kHz acoustic Doppler current profiler on the RV *Atlantis* during a February 2010 transit along 20° S. Embedded in the main thermocline with a vertical span of ∼500 m, the lens had an overall diameter of ∼150 km with a peak speed of 0.33 m s^{-1} at ∼35 km radius. Knowledge of the velocity field permitted determination of energetics and vorticity properties in detail. The ratio of potential to kinetic energy was ∼14, and the relative vorticity of the lens core was −0.7 times the local Coriolis parameter. Using a dynamically estimated density field, the potential vorticity of the lens's core was a factor of 6 less than the surrounding waters, the only source of which could be equatorial subsurface water. The lens had an estimated age of ∼4 years depending on where it was formed off the Peru-Chile coast. A search for similar lenses in the Argo database showed that they could be found throughout the southeast Pacific. Emanating from the southern Chile continental slope, their thickness-to-width aspect ratio decreased as they drifted west and equatorward. The inferred very slow rate of decay suggests that these rapidly spinning disks must be quite stable, but the thinning population suggests that they rarely get to live their full life cycle; more likely, they are torn apart by collision with other lenses or energetic mesoscale events.

Keywords. anticyclonic lenses, meddies, lens age, ADCP data, SE Pacific, Argo floats, eddy potential and kinetic energy

1. Introduction

Eddies and lenses (coherent vortices without evident surface expression) are commonplace in the ocean. This we know from Lagrangian methods, especially subsurface floats, which have been quite effective in documenting their presence across the North Atlantic (e.g., Rossby, Riser, and Mariano 1983; Richardson, Bower, and Zenk 2000; Shoosmith et al. 2005) and across the North and South Pacific (e.g., Johnson and McTaggart 2010; Chaigneau et al. 2011; Collins et al. 2013; Holte et al. 2013). When deployed in sufficient numbers, float trajectories suggest near-equal distribution of cyclonic and anticyclonic

1. Graduate School of Oceanography, University of Rhode Island, Kingston, RI.
2. Corresponding author address: GSO/URI, 215 South Ferry Rd., Narragansett, RI 02882-1197. ***e-mail: trossby@gso.uri.edu***

vortices (Shoosmith et al. 2005), that lenses can last several years (e.g., Armi et al. 1989), and that they can be found both in and below the main thermocline (Rossby et al. 1983; Elliot and Sanford 1986; Kassis 2000). One can also search for coherent eddy motion using acoustic Doppler current profilers (ADCPs) mounted in ships in transit. An example of this is the study by Luce and Rossby (2008) who developed and applied an algorithm for detecting velocity patterns consistent with axi-symmetric vortices. The situation is further simplified for those cases in which a vessel by good fortune cuts through the center of a vortex as happened for both an anticyclonic eddy and a cyclonic cold-core ring (Rossby et al. 2011). Rossby et al. (2011) were able to examine the dynamic properties of both eddies in some detail. A good share of our knowledge about coherent vortices comes from work in the North Atlantic, but it is still far from complete. There is still much to be learned about the mechanisms by which these eddies and lenses are formed, their life cycle and eventual demise, and thus what role they may play in the transport and redistribution of physical, chemical, and biological parameters across ocean basins. Although our knowledge of eddy populations and dynamics in other ocean basins is perhaps even more limited, Argo floats have proved to be effective at profiling the structure of the pycnostads and pycnoclines that characterize anticyclonic and cyclonic lenses, respectively. The study by Johnson and McTaggart (2010) gives an excellent survey of anticyclonic lenses in the southeast (SE) Pacific. The observed distribution of lenses strongly suggests that they originate off the southern coast of Chile. This is also a regional observation, and model studies show that the Peru-Chile Undercurrent (PCUC) can separate from the continental slope and produce anticyclonic eddies/lenses (Hormazabal et al. 2013).

The purpose of this article is to document in detail an anticyclonic lens that by good fortune was traversed right through its center by the RV *Atlantis* during a transit along 20° S in the SE Pacific Ocean. What makes this data set particularly compelling is the high quality of the ADCP data that reach down to 800 m through the entire core of the lens. Although we have not been able to identify any Argo profiles of this lens, the Argo archive provides an extensive database to search for similar structures. Johnson and McTaggart (2010) identified a corridor of lenses emanating from the southern Chilean coast, and we extend their work here to include some more recent profiles and to examine their properties. We also find evidence for a second source of lenses farther north along the Peru coast as had been noted before by Chaigneau et al. (2008). Section 2 gives a brief review of the data and methods used in this study. Section 3 is split into three parts: The first part details the velocity field of the lens from which a number of dynamic properties can be derived including its dynamic height, relative vorticity, and the lens's total potential and kinetic energy. The second part uses geostrophy to reconstruct a dynamically consistent density field of the lens, which will be used to assess how it may have evolved since its formation. The third part uses the Argo data set to search for other lenses and to establish their potential vorticity (PV) and salinity distribution patterns in the larger context of the SE Pacific circulation. The discussion (Section 4) uses these findings to attempt a synthesis of the most likely life cycle of the lens. A brief summary (Section 5) concludes the article.

2. Data and methods

a. The ADCP data and analysis methods

The ADCP data were obtained by the RV *Atlantis* during a transit along 20° S in February 2010. The 75 kHz data have been processed and are available at the NOAA ADCP website (http://ilikai.soest.hawaii.edu/sadcp/main_inv.html). The accuracy and spatial resolution of each 5-minute average of 150 pings was 0.013 m s^{-1}, 16 m in the vertical by 1.77 km in the horizontal. The accuracy of ADCP data depends crucially on the accuracy of concurrent vessel speed and heading measurements. The ship was equipped with an Ashtech ADU-5. This gave heading information accurate to 0.1°, which at a vessel speed of 12 kn meant a possible cross-track velocity error of 0.01 m s^{-1}. For the purposes of this study, these numbers are comfortably small. The conductivity, temperature, and depth (CTD) data were obtained courtesy of the chief scientists of the cruise, Prof. Douglas Capone and Dr. Troy Gunderson, University of Southern California. For further information on the principles of operation and use of a vessel-mounted ADCP, see, for example, Flagg et al. (1998).

Given knowledge of the velocity field, one can learn much about the dynamic structure of the lens. One can use the momentum equation "in reverse" to determine its dynamic height field, from which the potential energy integral can be determined, and its kinetic energy can be computed directly from the velocity field. The structure of the lens's density field follows directly from cross differentiating the radial momentum balance

$$-\frac{v^2}{r} - fv = -\frac{1}{\rho}\frac{\partial p}{\partial r} = \frac{\partial \Phi}{\partial r} \tag{1}$$

with the hydrostatic equation $0 = -\partial p/\partial z - \rho g$ to obtain the standard gradient wind equation in cylindrical coordinates:

$$\frac{\partial v}{\partial z}\left(\frac{2v}{r} + f\right) = -\frac{g}{\rho}\frac{\partial \rho}{\partial r} \tag{2}$$

where v is azimuthal velocity, ρ is density, f is the Coriolis parameter, r is radial distance from the center of the lens, and g is the gravitational constant. Both v and ρ are functions of radial distance and depth. Thus, integrating equation (2) across the lens for each and every depth gives the lens density field relative to a given density profile outside the lens. Similarly, Φ in equation (1) expresses the potential energy of a unit mass: $\Phi = gz = -p/\rho$ (Fofonoff 1962). Thus, integrating equation (1) for all z gives the radial distribution of geopotential field across the lens relative to a corresponding potential energy profile outside the eddy.

Multiplying Φ by ρ and integrating in the vertical, the potential energy of a water column per unit area relative to some background profile Φ_b is obtained as follows:

$$E_0 = \int_{z_r}^{z_S} \rho(\Phi_0 - \Phi_b)dz = \int_{z_r}^{z_S} \rho \Delta \Phi dz, \tag{3}$$

where the integral runs from a reference depth to the surface, and $\Delta\Phi$, a function of z and r, represents the departure of the observed geopotential surface from its background value at the same depth. To estimate potential energy per unit area for a layer, between the surface (s) and some selected depth (i), say, the reference depth is not needed:

$$E^{S-i} = \int_{z_r}^{z_S} \rho\Delta\Phi dz - = \int_{z_r}^{z_i} \rho\Delta\Phi dz = \int_{z_i}^{z_S} \rho\Delta\Phi dz. \tag{4}$$

A further integration across the eddy gives its total potential energy (TPE):

$$TPE = \int\int E^{S-i} dxdy. \tag{5}$$

"Total" indicates the potential energy created by the departure of the density field from a state of rest. This quantity can therefore be deduced from the velocity field only; no hydrographic data are required. It is positive in anticyclonic and negative in cyclonic eddies (Rossby et al. 2011). In order to obtain TPE of the lens, it is imperative to remove its mean velocity. Thus, the integral should be performed under the condition that the mean velocity of the lens normal to the plane of integration has been subtracted.

The total kinetic energy (TKE) in the eddy is obtained from the directly measured velocity field:

$$TKE = \int\int \left[\int_{z_r}^{z_S} \rho \frac{(u^2 + v^2)}{2} dz \right] dxdy, \tag{6}$$

where the external integral assumes that the velocity field decays to zero outside the eddy. In practice, some judgment must be exercised to decide where that cutoff should be.

These integrations will in principle be exact for steady circular flow because both terms of the left-hand side of equations (1) and (2) are known from the data. Thus, given Φ and velocity, one can determine the available potential and kinetic energy of the lens or eddy as a whole (Rossby et al. 2011; Søiland and Rossby 2013). The relative vorticity follows directly from the velocity field. Again, assuming rotational symmetry, we have

$$\zeta = \frac{v}{r} + \frac{\partial v}{\partial r}. \tag{7}$$

b. The Argo data and analysis methods

The Argo profile data provide an enormous wealth of information about the hydrography and circulation in the SE Pacific. They will be used here for both the large-scale description of the SE Pacific and to characterize individual lenses. Estimating the mean circulation on the $\sigma_T = 26.5$ kg m^{-3} density surface on which the lens was centered requires two steps. First, we estimate the Montgomery potential (MP), the stream function for fluid motion on

an isopycnal surface, specifically for $\delta = 1.68 \times 10^{-6}$ m^3 kg^{-1} specific volume anomaly surface (close to $\sigma_T = 26.5$ kg m^{-3}) relative to 1,000 dbars:

$$MP = p_\delta \delta - \int_{1000}^{p_\delta} \delta dp. \tag{8}$$

From this, we can obtain the corresponding baroclinic velocity field through differentiation. The 1,000 dbar reference velocity is obtained from the recent study by Ollitrault and de Verdiere (2014). Combining the two gives the absolute mean velocity, given here with a $5^\circ \times 5^\circ$ resolution. No attempt was made to resolve the very narrow south-flowing PCUC. The Argo data were also used to construct the mean thickness of the MP surface defined by the 26.2–26.8 kg m$^{-3}\sigma_T$ layer, the corresponding mean PV, $-f/\rho\partial\rho/\partial z$, and finally, the mean salinity distribution on the 26.5 kg m$^{-3}\sigma_T$ surface.

Following the approach used by Johnson and McTaggart (2010), we also used the Argo profile data to search for the presence and distribution of lenses centered on the $\sigma_T = 26.5$ kg m^{-3} surface. Lenses are easy to spot thanks to (1) the presence of a pycnostad, which significantly reduces the PV of the lens relative to the surrounding water (even without knowing its relative vorticity); (2) a concomitant dynamic height anomaly; and (3) a striking salinity maximum relative to the surrounding waters. All analyses used only adjusted Argo data, the expected accuracy of which is ± 2 dbars, $\pm 0.002^\circ$C, and $< \pm 0.01$ practical salinity units (PSU), respectively (Riser, Ren, and Wong 2008). The criterion used here for accepting a profile as a lens profile is that it had a dynamic height signal of at least 0.05 dynamic meters (dyn. m) relative to surrounding profiles on the $\sigma_T = 26.5$ kg m^{-3} surface, as well as a conspicuous pycnostad. The strongest lenses close to the Chilean coast had $\sim$0.2 dyn. m amplitude. The lenses were identified by visual inspection. A separate search identified nine floats exhibiting a distinct anticyclonic looping motion at their 1,000 dbar parking depth. These proved to be very useful.

3. Findings

The stimulus for this article comes from Figure 1, which shows a vertical cross section of meridional velocity as observed by the RV *Atlantis* during an east–west cruise along 20° S. At 93° W, a striking north–south velocity signal was centered near 330 m depth. It exhibited a 0.33 m s^{-1} peak velocity compared with a background root-mean square (RMS) velocity of $\sim$0.07 m s^{-1} at this same depth, so it was quite energetic, although one does see a fairly strong mesoscale feature with $>$0.2 m s^{-1} speeds near 86° W. In the first two subsections, we zoom in on the velocity field of the lens and use it to derive its dynamic properties, energetics, and the matching density field. The third subsection uses the Argo data to map out the mean fields of circulation, PV, and salinity on the $\sigma_T = 26.5$ kg m^{-3} surface and the corresponding lens properties on these surfaces.

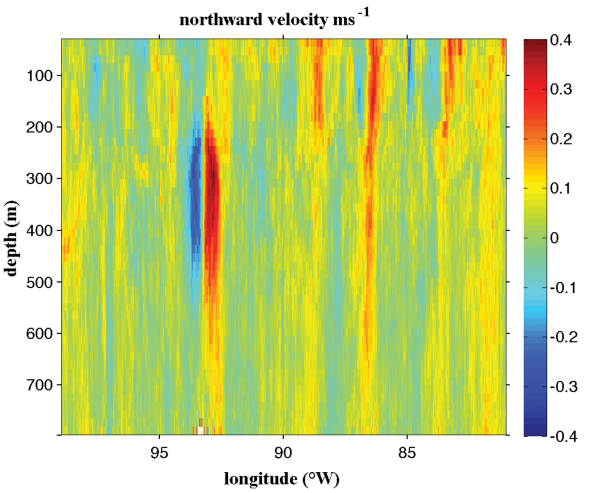

Figure 1. Meridional velocity along 20° S indicating good coverage of the acoustic Doppler current profiler to almost 800 m depth. It shows clearly an intense anticyclonic lens at 93° W and a mesoscale feature with ∼0.2 m s^{-1} speed near 86° W. The root-mean square eddy velocities were otherwise a factor of 5 less than the peak speed in the lens.

a. Lens dynamics and energetics

The location of the lens at 20° S, 93.3° W puts it on the northern side of the South Pacific subtropical gyre such that the mean flow at the depth of the lens was estimated to be northwestward at ∼0.01 m s^{-1} (section 3d). The geographic aspects of the lens are given in in the next subsection. Figure 2 (left panel) shows the vertical and lateral extent of the lens as transited by the RV *Atlantis* along 20° S: 150–650 m depth (∼500 m thick) and an overall diameter of ∼150 km making this one of the thinnest aspect ratio lenses observed to date. The right panel of Figure 2 shows a maximum swirl velocity of 0.33 m s^{-1} at ∼330 m depth. The almost complete absence of any zonal velocity component indicated that the lens was bisected nearly perfectly along its diameter; the lens center was ∼4 km north of the vessel track. At the time of encounter, its mean velocity was ∼0.04 m s^{-1} to the north; this mean drift has been removed so that the east–west symmetry of the lens stands out clearly in these panels. It has also been removed in all subsequent analyses.

To provide a quantitative measure of lens size and intensity, the first derivative of an assumed Gaussian stream function was fitted to the velocity field at a number of depths. The left panel of Figure 3 shows that the fit worked quite well such that the RMS difference between the two was ∼0.04 m s^{-1}. Most of the misfit is assumed to be due to small-scale (internal waves, inertial motion?) activity and not due to the functional form used in the fit, although the velocity gradient was somewhat steeper within 12 km of the center of the lens as shown by the solid line. No filtering has been applied, and tidal velocities are expected to be small in the middle of the ocean. Although the Gaussian stream function gave a good fit

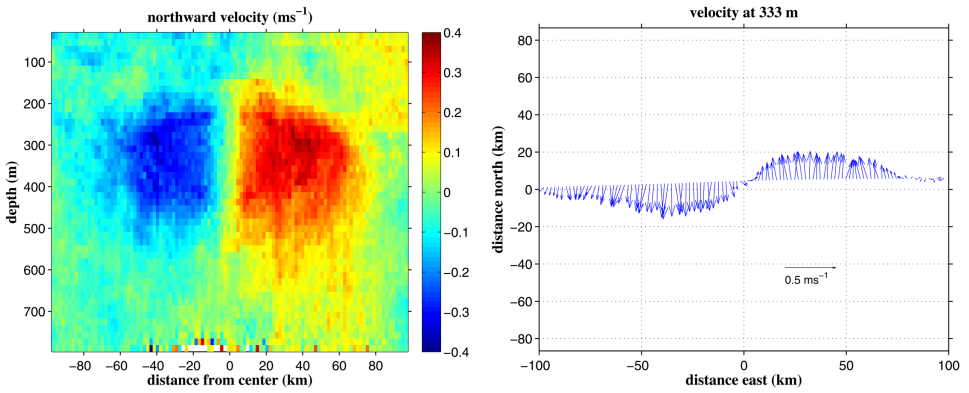

Figure 2. Vertical cross section along 20° S through the lens of north–south velocity (m s^{-1}) (left panel). The pixel size is 1.7 km × 16 m. Velocity vectors at 333 m depth along the vessel track (right panel).

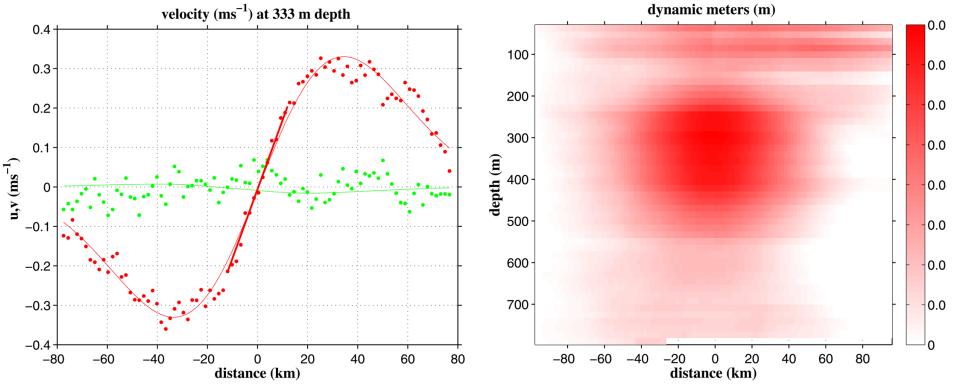

Figure 3. Velocities at 333 m depth relative to the center of the lens and the corresponding fit of a Gaussian stream function to the data (left panel). The solid red line at the center is a local linear fit indicating the solid body slightly steeper than Gaussian velocity gradient there. The dynamic height anomaly field (expressed in dynamic meters) obtained by horizontal integration of the momentum equation from a motionless density profile at the left edge of the figure (right panel).

at all depths in the lens, the estimated radius increased substantially with depth from ∼29 km at 109 m depth to 74 km at 685 m (Table 1). Significantly, the velocity residual in the last column of Table 1 appeared to be insensitive to the amplitude of the lens. As noted earlier, the RMS velocity at the depth of the lens along 20° S was 0.074 m s^{-1}. This included all spatial scales and timescales that can be resolved by the 1.77 km and 5 min averaging that went into each profile.

The dynamic height anomaly Φ throughout the lens can be estimated directly from the velocity field integrating equation (1) (right panel of Fig. 3). Expressed as steric height,

Table 1. Gaussian stream function fits to the lens velocity field at selected depths. Bold rows highlight the core of the lens. A, v-max, and v-residual represent the amplitude of the fitted function, maximum swirl velocity and root-mean square scatter around the fit, respectively.

Depth (m)	Radius (km)	A (m^2 s^{-1})	v-max (m s^{-1})	v-residual (m s^{-1})
109	29	−3,500	0.10	0.037
173	34	−6,000	0.15	0.039
205	35	−9,500	0.23	0.040
269	**49**	**−18,500**	**0.32**	**0.041**
333	**48**	**−18,500**	**0.33**	**0.033**
397	**46**	**−16,900**	**0.32**	**0.042**
493	50	−10,000	0.17	0.051
589	56	−6,400	0.10	0.031
685	74	−5,000	0.06	0.074
749	80	−5,000	0.05	0.063

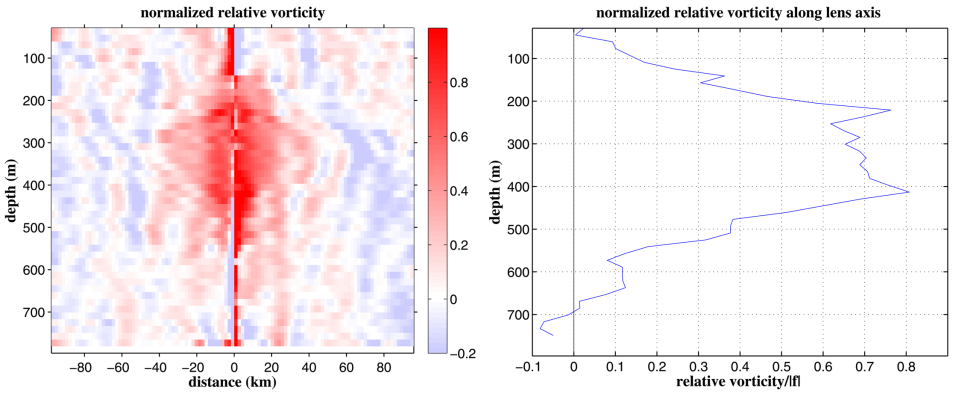

Figure 4. Vertical cross section of normalized relative vorticity (left panel). Vertical profile of normalized relative vorticity at the center of the lens estimated from a linear least-square fit of velocity of for $|x| < 10$ km (right panel).

it reaches a maximum of 0.079 m at 333 m depth relative to the surrounding water. This quantity is geostrophically equivalent to estimating the dynamic height field by integrating specific volume in the vertical, the difference being that Φ reflects the full velocity field of the lens, whereas the classical method typically assumes a level of no motion at some depth.

The relative vorticity of the lens normalized by the local Coriolis parameter f reveals an intense anticyclonic core that reached a maximum of $-0.7f$ between 200 and ∼500 m depth (Fig. 4, left panel). Outside the central core of the lens, the vorticity did not decrease monotonically with increasing radius but exhibited vertical bands of alternating vorticity ($\pm 10\%$ of f) to nearly the maximum radius of the lens. The extreme values at the center

reflect the difficulties of estimating the two terms in equation (7) at small r plus the fact that the lens axis evidently was not perfectly vertical. However, under the assumption of solid body rotation at small radii ($x < \pm 10$ km), one can also obtain the vertical distribution of relative vorticity field by means of a least-square fit of a linear function: $v = \partial v/\partial x \cdot x$ to the observations for each and every depth. This leads to a profile of relative vorticity for the center of the lens as shown in Figure 4 (right panel). The core of the lens exhibited some striking features that have been seen elsewhere (Rossby et al. 2011), namely a weak but clear increase in intensity with depth bounded by thin layers of even greater relative vorticity at the top and bottom of the core, beyond which it rapidly decreased. The "solid body" core of the lens core had a 4-day rotation period.

The estimation of both TPE and TKE from equations (5) and (6) is quite straightforward, but it is imperative to remove the mean velocity of the lens in order to obtain accurate numbers for the lens itself; this was particularly true for TPE. The TPE and TKE integrals equaled 2,168 and 151 terajoules (TJ), respectively, with a ratio of ∼14.

b. Estimated density field of the lens

The dynamic method has been used extensively to determine the velocity fields and oceanic transports from hydrography. The same approach applies here, except in reverse, namely to use the momentum balance to infer the density field consistent with the observed velocity field. However, as the measured velocity includes motions over a continuum of timescales and spatial scales, it becomes necessary to low-pass filter the profiles to remove ageostrophic contributions to the velocity field. The method is arbitrary in the sense that no a priori information is available on the vertical scales and depths at which the motional field may not be geostrophically balanced; the same applies to the horizontal structure of the velocity field. Lacking a formal approach, we low-pass filtered the vertical profiles to attenuate all velocities on vertical scales less than ∼40 m (∼160 m wavelength). These smoothed profiles were then integrated eastward from a reference profile (constructed from a set of Argo profiles) at 94.25° W, ∼100 km west of the lens center to obtain the density field shown in Figure 5. As expected for an anticyclonic lens, a conspicuous pycnostad is observed at its center with a sharp density gradient above and a weaker one below. Delimiting the core of the lens by the 26.2–26.8 kg m$^{-3}\sigma_T$ range, the stratification decreased by a factor of 2 relative to the surrounding water. This, coupled with the reduction in absolute vorticity ($f + \zeta$) magnitude from f to $0.3f$, a factor of 3, meant that the PV of the core was a factor of 6 less than the surrounding water. Because PV is a conservative quantity, it can be quite helpful as a tracer especially as we do not have any information on the core's temperature/salinity (T/S) characteristics.

c. The Argo hydrographic picture

Following Johnson and McTaggart (2010), we revisited the growing Argo database to locate similar lenses that can be used to study how lenses migrate and age after their genesis

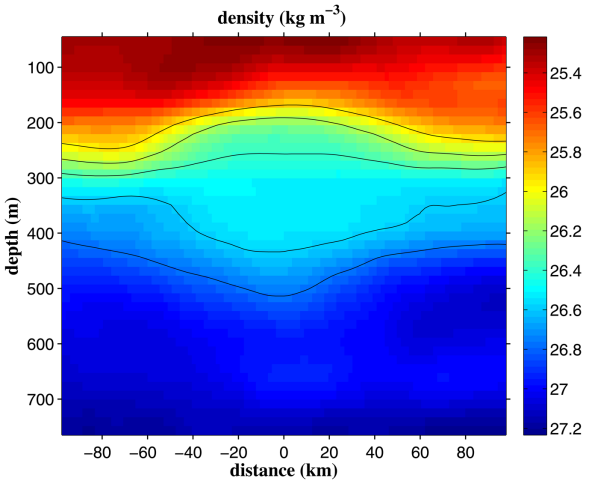

Figure 5. The σ_T (kg m^{-3}) field of the lens estimated from the velocity field through the application of reverse geostrophy (see text). The lines indicate σ_T contours between 26.0 and 26.8 in 0.2 kg m^{-3} steps.

near the Chilean coast. To put these into the larger context of circulation and property distributions, we show their distribution and properties on (1) the mean circulation field, (2) the mean PV field, and (3) the mean salinity field, all on the $\sigma_T = 26.5$ kg m^{-3} surface. This isopycnal surface was representative of the surface on which the lens "floated" (see Fig. 5), meaning that this surface was essentially level within the lens, with shallower and deeper surfaces bulging up and down, respectively, thereby creating its pycnostad. We will also show that this isopycnal surface was representative of the core of all 55 lens sightings used in this study.

The Argo float trajectories and T/S profiles were used to construct the mean circulation shown in Figure 6. The color field shows the MP, and the vectors give the mean velocity field. The vectors are largely parallel to the MP just as the reference velocity field at 1,000 dbars (Ollitrault and de Verdiere 2014) tends to parallel the baroclinic shear as well. The general circulation is clearly that of the wind-driven South Pacific subtropical gyre (e.g., Talley et al. 2011). The figure also includes the trajectories of nine Argo floats that clearly exhibited "looping" motion (Shoosmith et al. 2005) associated with coherent eddy motion. We will return to these looping floats in the discussion.

PV, $-f/\rho\partial\rho/\partial z$, is a very useful dynamic tracer. For the large scale, we apply it directly to the $\sigma_T = 26.2-26.8$ layer. For lenses, there are two problems. First, of course, we cannot determine their relative vorticity with single profiles, and second, we do not know a profile's distance from the center. This means that the profiles will to some degree underestimate the vertical extent and stratification of its pycnostad. This limited us to selecting profiles with very weak stratification or equivalently a large dynamic height anomaly relative to

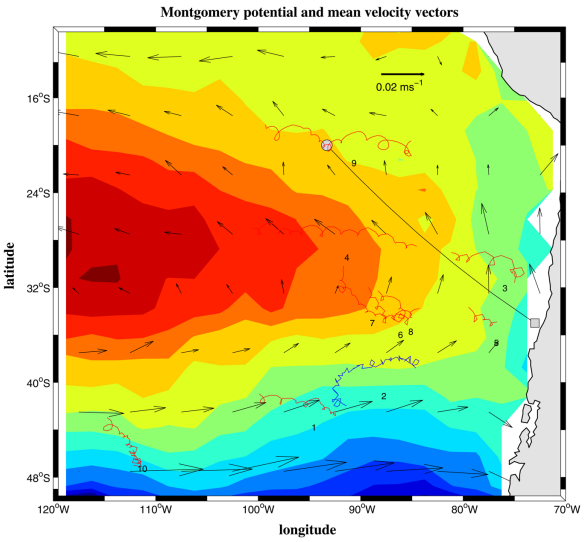

Figure 6. The Montgomery potential expressed in dynamic meters on the $\delta = 1.68 \times 10^{-6}$ m^3 kg^{-1} surface (close to σ_T = 26.5 kg m^{-3}) relative to 1,000 dbars. Vectors show the mean velocity (m s^{-1}) on this surface estimated from the Montgomery potential and the mean circulation at 1,000 dbars. The trajectories are those of Argo floats trapped for a period of time in a lens.

previous and subsequent profiles, and although this did not guarantee that they caught the full anomaly of the lens, the method seemed to work well. It is assumed that the lenses were of comparable strength at the time of formation, which we think is reasonable assuming that they result from the pinch off of the PCUC in situations where it separates from the continental slope (Hormazabal et al. 2013). A search through the Argo database corroborated the finding by Johnson and McTaggart (2010) that profiles with a well-developed pycnostad can be found throughout the SE Pacific corridor they identified. Figure 7 (left panel) shows the location and thickness of the 26.2–26.8 kg m$^{-3}\sigma_T$ layer in each lens. The very thickest ones (dark red) can be found just off Chile between ~30° and 40° S with layer thickness decreasing with increasing distance to the north and west. The solid circle at 20° S, 93.3° W indicates our lens with its estimated 330 m maximum layer thickness; it was representative of the thicker lenses in the vicinity (but recall that some Argo profiles will underestimate layer thickness because they miss the center of the lens). The lens thicknesses are plotted on the mean stratification defined by the same 26.2–26.8 kg m$^{-3}\sigma_T$ layer using the same Argo database. As expected, all lenses have significantly weaker stratification than the surrounding water. These must emanate from the PCUC that hugs the continental slope because this is the only source of low-PV water in the SE Pacific on this density surface, as indicated by the 500 m long bar at the right in Figure 8 (adapted from Hormazabal et al. [2013]). The figure also shows a lens with a ~450 m thick layer, almost as thick as the PCUC itself. The 5° × 5° spatial resolution used for Figure 7 did not permit us to map

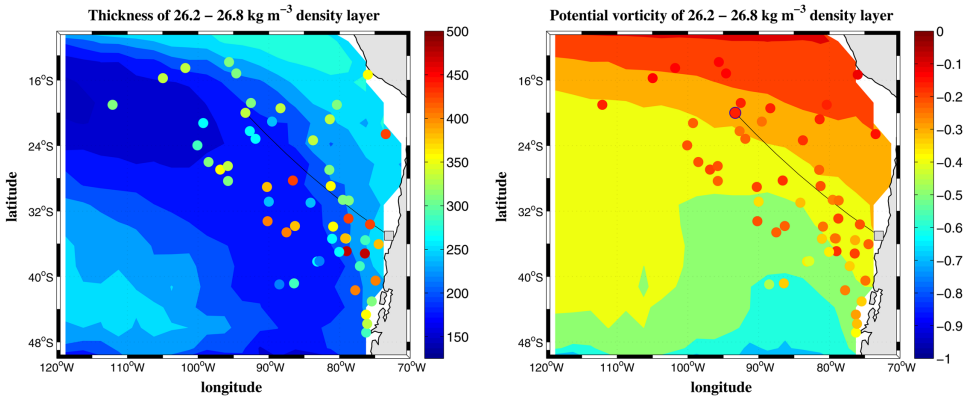

Figure 7. Layer thickness (m) of the 26.2–26.8 kg m$^{-3}\sigma_T$ surface and the thickness of the 55 lenses found in the Argo database (left panel). The corresponding potential vorticity in units of 10^{-9} m^{-1} s^{-1} (right panel). The gray box and line represent a hypothetical origin and shortest path of our lens.

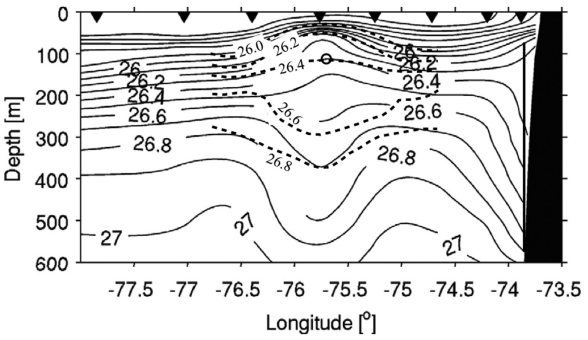

Figure 8. Hydrographic section along 37.33° S extending west from the Chilean coast (adapted from Fig. 2 in Hormazabal et al. [2013]). The solid lines show density in 0.1 kg m$^{-3}\sigma_\theta$ steps. The dashed lines show the 26.2–26.8 kg m$^{-3}\sigma_T$ density lines copied from Figure 5. They have been lifted ~140 m to align the 26.4 kg m^{-3} surfaces at the circle. The lens (solid lines) was 450 m thick compared with our 330 m. The 500 m long line on the right highlights the thick 26.2–26.8 kg m$^{-3}\sigma_\theta$ layer at the continental slope.

out this narrow boundary current with its weak stratification. The PV, $-f/\rho\Delta\rho/\Delta z$, of the 26.2–26.8 σ_T layer had a similar but more zonal orientation due to the rapid decrease in f toward the equator (Fig. 7, right panel). This same quantity, $-f/\rho\Delta\rho/\Delta z$, is computed and plotted for the lenses. However, because this does not include their relative vorticity, their actual PV might be up to 3 less in magnitude as indicated by the $-0.7f$ relative vorticity of our lens. Now the connection to the south-flowing PCUC with its low-PV equatorial subsurface water farther north becomes a bit more evident because there is no other source of low-PV water in this density range.

Table 2. Summary of lens drift vectors.

No.	Longitude (° W)	Latitude (° S)	Speed (m s^{-1})	Heading (° T)
1	95.8	41.8	0.014	283
2	89.0	39.2	0.012	237
3	77.2	30.0	0.022	294
4	92.6	27.5	0.036	273
5	78.0	34.7	0.026	298
6	87.4	34.0	0.023	305
7	90.1	33.0	0.018	321
8	86.4	33.7	0.018	293
9	91.9	19.5	0.015	274
10	112.8	45.3	0.011	335

The mean velocity vectors in Figure 6 suggest a 0.01 m s^{-1} average speed along the presumed path of our lens. If the lens is passively advected along this 2,600 km great circle path from an assumed starting point at 35° S, 73° W (the curved line in this and following figures), its age would be ∼8 years old. However, considerable evidence suggests that the lens may be moving faster than this. The same figure also shows the trajectories of 10 Argo floats that exhibit "loopy" motion as they translate. The red anticyclonic "loopers" drift toward the west-northwest in a rather straight manner, whereas the single cyclonic (blue) looper drifts as expected poleward. Table 2 summarizes their drift characteristics. The rather linear drift of these floats compared with the more wandering character of floats not trapped in loopers (not shown) points to an active control or propulsion mechanism.

Although the tracks of the three floats (3, 4, and 9) closest to the presumed track of our lens are more zonally oriented, we might use their 0.024 m s^{-1} mean speed as a measure of their actual rate of translation. Dividing this into the 2,600 km distance leads to ∼3.4 years as the age for the lens. If we use the speed component parallel to the presumed lens track, then the age increases to ∼3.7 years. Figure 6 also shows a strong northward flow just west of the Chilean coast. This together with the presence of some lenses in the north suggests that a likely route was more northerly at first after which it drifted more zonally as indicated by these tracks. This added path length would further increase its age somewhat. As an aside, the looping period of these floats was ∼30 days or more with speeds increasing with radius from 2 to <5 km d^{-1} at the most, which meant they were not strong compared with the ambient eddy field. Although the ADCP data did not reach to 1 km depth, the velocity field at 700–800 m depth showed a weak anticyclonic pattern that may well extend another 200 m or more. There is no reason to think that this eddy could not trap an Argo float, at least for a while; all that is required is that the fluid surrounding the lens not move past it faster than the looping velocity so that there exists a closed domain underneath the lens at that depth (Flierl 1981). In what follows, it is assumed that the lens was at least 3 and more likely closer to 4 years old.

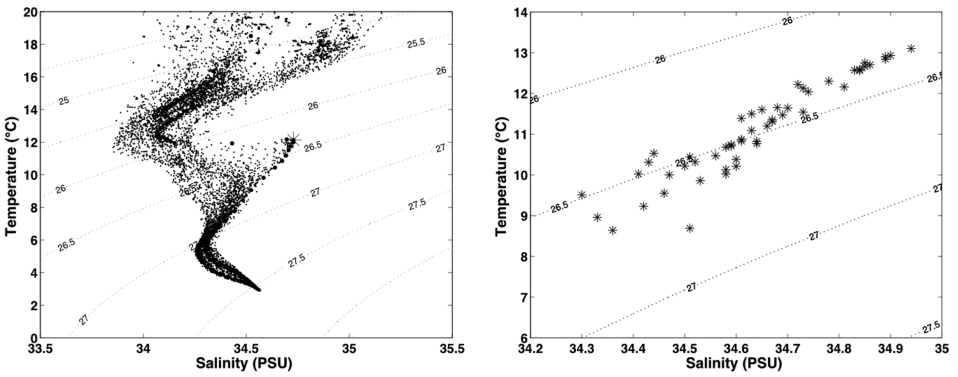

Figure 9. Temperature/salinity (T/S) diagram of all profiles from float 3 in Figure 6 (left panel). The solid dots indicate the profile closest to the center of the lens. The star marks the most extreme T/S value. Summary plot of the T/S extrema from the 55 lenses identified in this study (right panel). PSU, practical salinity units.

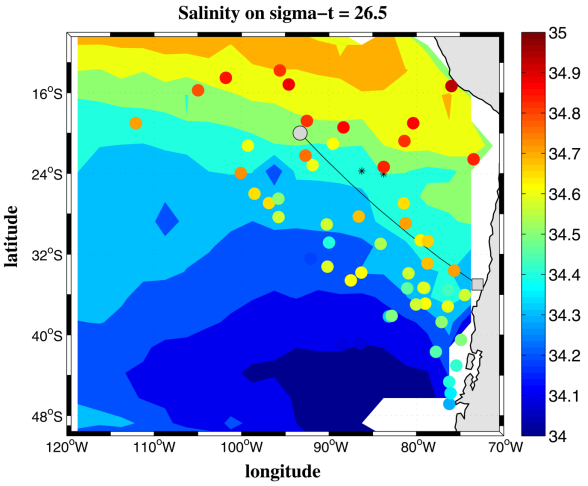

Figure 10. Salinity on the $\sigma_T = 26.5$ kg m^{-3} surface and the salinity extrema in each of the lenses (on this same surface). The gray box and line represent a hypothetical origin and shortest path of our lens.

The Argo profilers also give us valuable information on the T/S properties of the lenses. Interestingly, the pycnostads exhibited salinity extrema in a very narrow density range (Fig. 9). The left panel shows the T/S diagram for all profiles from float 3 in Figure 6. The extrema in T and S peak at $\sigma_T = 26.4$ kg m^{-3} in the pycnostad when the float is profiling the center of the lens. The right panel shows the ensemble of extrema from all 55 lenses indicating the narrow range around $\sigma_T = 26.5$ kg m^{-3}, with somewhat lower σ_T at higher salinities and vice versa. Figure 10 shows the spatial distribution of the salinity extrema. It reveals

a rather well-defined organization of fresher to saltier lenses from south to north that is maintained even as they drift west from the continent. The spread of highly saline lenses in the north points to another source located perhaps somewhere between 16° and 22° S. Our lens is bracketed by red and yellowish lenses north and south of it making it unclear to which group it belongs. In any event, the figure suggests that the lenses to the northwest may not all originate from the southern Chilean coast. This is further corroborated by Figure 4 in Hormazabal et al. (2013), which shows two hydrographic sections following the PCUC along the Chilean continental slope from 31° to 41° S. These sections showed a weakening of salinity in equatorial subsurface water from ∼35.7 to 35.5 PSU over this latitude range. A number of well-defined lenses with even lower core salinities were found as far south as 48° S suggesting that lenses can be formed from the PCUC over a wide range of latitudes, but we cannot preclude the possibility of other sources of eddies or lenses where this density surface outcrops farther south. Because we do not know the salinity of our lens, we cannot be sure; however, given the orientation of the float tracks, we will assume that our lens came from off the Chilean coast.

The salinity anomalies appeared to remain intact as the lenses drifted west-northwest. Orange lenses (S ∼34.7 PSU) as far west as 100° and 112° W and a red one west of 100° W suggest that the core of the lens remains unaffected since its formation off Chile and Peru. This is in accordance with other studies indicating that the core of a lens can remain untouched by the surrounding water for several years as its drifts through the ocean (e.g., Armi et al. 1989; Prater and Rossby 1999). An undiluted salinity anomaly also supports the earlier expectation that the PV anomaly of a lens remains intact even as it thins during its transit north and west into a lower-PV environment.

4. Discussion

A comprehensive analysis of altimetric data by Early, Samelson, and Chelton (2011) shows clearly that anticyclonic features tend equatorward and vice versa for cyclones. They also show that their speed is best approximated by the phase speed in the direction of the first baroclinic mode planetary wave propagation, notwithstanding the finite size of these coherent features. However, what about internal lenses such as the one studied here, whose internal structure cannot be described by a single flat-bottom baroclinic mode, the closest one of which (no. 2) sits far too deep in the water column and has far too small a radius of deformation (Fig. 11). Nof (1981, 1982) proposed that the speed of a lens is $U \sim \beta R_d^2$, where $\beta = \partial f/\partial y$ and R_d is the radius of deformation $\sqrt{(g'h)}/f$ and h is the vertical scale of the lens. Although much has been written on the question of lens self-propulsion (e.g., McWilliams 1985; Cushman-Roisin, Chassignet, and Tang 1990; Nycander 2001), for the purposes of this article we find Nof's expression to be quite effective. It can be rewritten as $U \sim \beta \mathrm{Ro} L^2$, where L is a characteristic scale for the lens and Ro is the Rossby number, which besides expressing the intensity of the lens can be determined directly from the ADCP velocity data. Because the Argo trajectories give us a good estimate of lens speeds, but little

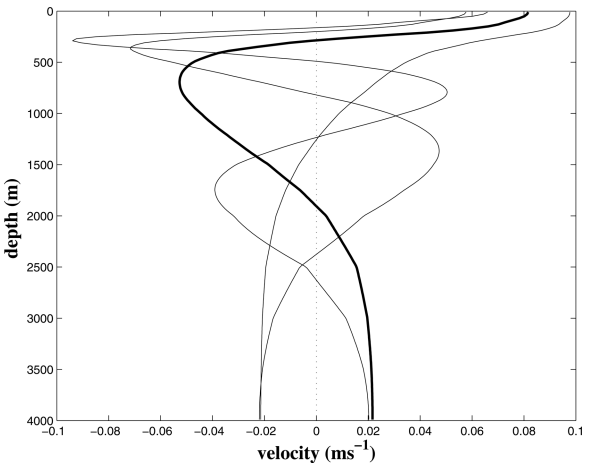

Figure 11. Flat-bottom velocity modes for a typical density profile near the lens. The deformation radii for modes 1–4 are 134, 41, 15, and 8 km, respectively. The second mode (thick black line) comes closest to resembling the lens velocity profile but is much too deep.

information on their sizes, we can use this expression to estimate the effective size of the lens. Using the $U = 0.02$ m s^{-1} average velocity for the three floats near the presumed track of the lens, Ro $= 0.7$, and $\beta 2 \times 10^{-11}$ s^{-1} m^{-1}, we obtain $L = 38$ km, comparable to the ∼35 km radius for maximum velocity (Fig. 3, left panel). However, this calculation assumes that the lens is translating independent of the background flow, a supposition that was not supported by the range of observed lens speeds. Figure 6 and Table 2 show lenses 3, 4, and 9 in the north moving faster to the west than the other lenses farther south that do not have this "advective" advantage. If we remove this ∼0.01 m s^{-1} westward advection from floats 3, 4, and 9, their self-propulsion speed drops to ∼0.01 m s^{-1} and the corresponding lens radius increases to ∼49 km, which, curiously, is similar to the Gaussian scale of the lens. Similarly, if we posit that lens 10 was bucking the eastward flow at ∼0.005 m s^{-1} such that its relative speed was ∼0.025 m s^{-1}, the scale of this lens will be about the same at ∼48 km (in both cases, Ro was assumed the same, 0.7; however, given its location, the origin of this southerly lens may be quite different). Although the size similarity was coincidental given the quality of the speed estimates, it suggested an underlying narrow range for the size of the lenses. However, the main point here is that the speed at which lenses move depends not only on β as for planetary waves, but also on their size and advection by the environment in which they are embedded.

The fact that our lens appeared to be so strong after nearly 4 years raises questions about how it ages and eventually dissipates or breaks up. A first question might be its change in size. Assuming that all lenses start off with similar dimensions, we superimpose our lens on the recently formed one shown in Figure 8. According to Figure 2b in the Hormazabal

et al. (2013), it appears that the section passed just north of the center of the lens, so for the purposes of this study, we will assume that the section was representative of the core of the lens. The dashed lines from our lens shows that its thickness has decreased ∼120 m from 450 to 330 m, much of it through shoaling from below such that the stratification on the bottom side of the lens increased. At the same time, the deepening of 26.6 kg m^{-3} surface relative to the top side of the lens suggested a thickening of the lens's pycnostad. This might accord with the near-solid body rotation of the core of our lens between 220 m and 420 m depth or equivalently for 26.3 kg m^{-3} $< \sigma_T <$ 26.6 kg m^{-3} (Fig. 4, right panel).

The northwestward drift of the lenses moved them into more highly stratified water. At the same time, the lenses became thinner and wider. The thinning of the mean 26.2–26.8 kg m^{-3}σ_T-layer thickness (from ∼250 to ∼190 m, a 24% decrease) and the decrease in the Coriolis parameter f from the lens in Figure 8 to ours (37.3° S to 20° S, a 44% drop) means that the anticyclonic lenses were drifting toward a lower f/h environment (Fig. 7, right panel). It would be interesting to know how the relative vorticity of the core has changed over time; at most, the relative vorticity could have been $+f$ after it had equilibrated post its formation due to inertial instability considerations (Holton 1992). As the lens drifted northwest, the PV $(f + \zeta)/h$ of the "solid body" rotating core should remain constant. Using this constraint and the Hormazabal et al. (2013) eddy in Figure 8 as a proxy for our lens soon after formation, the relative vorticity of the core might have been $\zeta_f = h_f(f + \zeta)/h - f_f$, where the subscript $f$refers to "at formation." Setting $h_f/h = 450/330$, we obtain $\zeta_f \sim 0.77 f_f$ meaning that ζ/f has decreased only ∼10% over the 4 years. The angular velocity, on the other hand, has decreased significantly such that the rotation period has more than doubled from 1.65 to 4 days during its equatorward movement.

The simultaneous widening of the lens as it thins points to a compensation process such that the rate of volume loss is less than that indicated by the thinning alone. A visual comparison of the lens off Chile and ours suggests that the top part of the lens remained roughly the same over its presumed 4-year drift; hence, there was little erosion from above. The change in lens shape and volume loss takes place primarily on the bottom half of the lens. If we postulate that the 120 m thinning applies to the bottom half, and further assume that the center of the lens is at ∼200 m (between the up- and down-bending isopycnals), then the σ_T = 26.8 kg m^{-3} surface has shoaled from 500 to 380 m depth (i.e., the lower half has thinned from 300 to 180 m). It is more difficult to judge the expansion in width, but it cannot be more than $\sqrt{}$(300/180) or ∼30% for a shape-preserving volume not to increase. Figure 8 suggests that the lens has broadened by something similar implying minor volume loss, but the lack of resolution in the hydrographic section (and the fact that we do not really know if it is a good proxy) limits us to conclude that the volume loss was somewhere between negligible and 120/300 of its lower half volume. Again, this and other calculations using the lens off Chile as a proxy for our lens not long after its formation must be viewed as suggestive only.

How do these lenses age, weaken, and eventually disappear, especially as the core of the lenses remains untouched in terms of its PV and salinity anomaly? In the case of the meddy "Sharon" that was studied over a 3-year period (Armi et al. 1989; Hebert, Oakey, and Ruddick 1990; Schultz Tokos and Rossby 1991), the core remained intact while intrusive layers from the sides and below completely obliterated the core of the lens over that time. In contrast, the original meddy that was observed off the Bahamas (McDowell and Rossby 1978) originated at the northwest corner at 51° N, 44° W if one accepts the conjecture of Prater and Rossby (1999). They estimated that the lens may have travelled >4,000 km distance in 3 years thanks to advection by the return flows offshore of the North Atlantic Current and Gulf Stream. However, just as important and unlike the erosion of the meddy "Sharon," this original meddy was quite large and thin with an aspect ratio comparable to our lens.

Can internal friction play a role in their aging? That would seem unlikely if, as they drift, they only change shape but not volume. However, let us suppose that our lens had thinned without broadening. The volume loss would be $\sim$120 m $\times 2\pi \int r \exp(-r^2/R^2)dr$ (with $R \sim 48$ km) $= 900 \times 10^9$ m^3 or equivalently in mass $\sim 0.9 \times 10^{15}$ kg. Because we do not know its TPE at genesis, let us assume that the loss of TPE scales with the loss of volume (i.e., 120/500 $\times$ 2,300 TJ over a 4-year period). These numbers result in a "bulk" internal dissipation rate $\varepsilon = 5 \times 10^{-9}$ W kg^{-1} within the eroding part of the lens. This is a factor of 5 to 10 larger than direct measurement estimates of ε. For example, Moum et al. (1995) obtained $\sim 10^{-9}$ W kg^{-1} at 175 m depth on the equator at 140° W, and Mori et al. (2008) obtained values $\sim 3 \times 10^{-10}$ W kg^{-1} in the North Pacific subtropical mode water. Although our dissipation estimate is necessarily approximate, it does not support the eroding volume assumption and instead reinforces the previously discussed view that instead of losing volume the lens primarily became thinner as it drifted into a lower-PV environment. Thus, the question about how these SE Pacific lenses age and disappear remains.

The ratio of maximum swirl velocity to the RMS eddy velocity field was O(5) suggesting a high level of immunity to disruption. However, some possibilities for disruption exist. First, as the lenses become thinner, they eventually become unstable (McWilliams 1985). A possible indicator of this is the Burger number, $B = (NH/fL)^2$, where N refers to the Brunt-Väisälä frequency and H and L are the vertical and horizontal scales of the lens. Using $\Delta\rho/\rho = 0.6/1026$ and $H = 300$ m for the core of the lens, and $L = 2 \times 35$ km, then $B \sim 0.14$. This is a small number, but if it exists, we do not know what a critical value might be. Perhaps this lens was getting close to a critical size and eventual breakup. Another reason may be that the thinning population results from lens collisions resulting in a loss of both (with some splintering into smaller lenses). Alternatively, transient or episodic mesoscale events such as the $\sim$30 km wide flow at >0.2 m s^{-1} at 86° W (Fig. 1) might shear a lens apart. Finally, as the lenses drift equatorward, they enter a region of increased shear associated with the South Equatorial Current. The lenses are now so large that the deformation imposed by the shear may render them unstable or tear them apart. In any event, unlike the meddy "Sharon," which was effectively wiped out over a 3-year

period, the lenses formed in the SE Pacific from instabilities of the PCUC off Chile show little evidence of decay over the multiyear timescales associated with their drift northwest into the South Pacific subtropical gyre. We still do not know what sets their life length. At an overall drift rate of 0.02 m s^{-1}, the lens at 112° W would be 6–7 years old, so clearly lenses could remain vital for many years. Instead, something interrupts them; at present, it appears that collision or distortion by mesoscale lateral shear is the best candidate.

5. Summary

The lens traversed by the RV *Atlantis* in February 2010 most likely originated from the PCUC somewhere between ∼30° and 40° S. The ADCP transect revealed a well-defined 300 m thick core in essentially solid body rotation to a radius of ∼12 km, above and below which the velocity and vorticity field rapidly decreases. As has been observed elsewhere, the top and bottom sides of the core have thin layers with even greater relative vorticity. What these represent is not known—perhaps (Ekman) boundary layers bracketing the core. Bands of alternating vorticity were seen out to the ∼75 km maximum radius of the lens. Examination of data from Argo profilers distributed throughout the SE Pacific revealed numerous similar lenses with distinct pycnostads and strong salinity anomalies of equatorial subsurface water origin. Using a cross section of a lens off Chile as a proxy for this lens shortly after genesis and given the distance to our lens, we estimate that it was close to 4 years old. Water within the lens will have made many hundreds of revolutions suggesting that lenses are inherently very stable and long lived. However, the thinning population to the northwest indicated that the lenses rarely live their full potential life. Instead, they meet their end either through collision with other lenses, lateral shear, or episodic mesoscale events. It could be quite interesting to undertake repeat ADCP and expendable CTD probe surveys of a lens's velocity and vorticity structure, radial symmetry, and radiation patterns using acoustically tracked subsurface floats to determine their drift patterns in detail and to relocate them for subsequent surveys. The quiet SE Pacific subtropical gyre provides what might considered a perfect laboratory setting to study the formation, dynamics, and life cycle of lenses.

Acknowledgments. My sincerest thanks go to Dr. Jules Hummon for bringing the ADCP cross section of the lens at 20° S to my attention; this has been an interesting study! My thanks also go to Drs. D. Capone and T. Gunderson of the University of Southern California for sharing the data from their cruise At 15-61. The processed data are available at the official National Oceanographic Data Center shipboard ADCP site (http://ilikai.soest.hawaii.edu/sadcp/main_inv.html). The Argo float data used here were collected and made freely available by Argo (http://www.argo.net/), a program of the Global Ocean Observing System, and contributing national programs. My colleague Prof. Peter Cornillon made my life easy by sharing the global Argo data set he had organized for his class in physical oceanography. I thank Drs. M. Ollitrault A. C. de Verdiere for a digital copy of their global circulation field, and Drs. G. Johnson and McTaggart for additional information on their paper; the Meteorological Institute at the University of Stockholm where most of the work and writing of this article were done; Prof. J. Nycander and Dr. L. Chafik for stimulating discussions; Dr. Chafik for teaching me how to prepare the maps in the figures; and finally, the two anonymous reviewers for very helpful comments and suggestions.

REFERENCES

Armi, L., D. Hebert, N. Oakey, J. F. Price, P. L. Richardson, H. T. Rossby, and B. Ruddick. 1989. Two years in the life of a Mediterranean salt lens. J. Phys. Oceanogr., *19*, 354–370.

Chaigneau, A., A. Gizolme, and C. Grados. 2008. Mesoscale eddies off Peru in altimeter records: Identification algorithms and eddy spatio-temporal patterns. Progr. Oceanogr., *79*, 106–119.

Chaigneau, A., M. Le Texier, G. Eldin, C. Grados, and O. Pizarro. 2011. Vertical structure of mesoscale eddies in the eastern South Pacific Ocean: A composite analysis from altimetry and Argo profiling floats. J. Geophys. Res.: Oceans, *116*, C11025. doi: 10.1029/2011JC007134

Collins, C. A., T. Margolina, T. A. Rago, and L. Ivanov. 2013. Looping RAFOS floats in the California Current System. Deep Sea Res., Part II, *85*, 42–61.

Cushman-Roisin, B., E. P. Chassignet, and B. Tang. 1990. Westward motion of mesoscale eddies. J. Phys. Oceanogr., *20*, 758–768.

Early, J. J., R. M. Samelson, and D. B. Chelton. 2011. The evolution and propagation of quasi-geostrophic ocean eddies. J. Phys. Oceanogr., *41*, 1535–1555.

Elliot, B. A., and T. B. Sanford. 1986. The subthermocline lens D1. Part I: Description of water properties and velocity profiles. J. Phys. Oceanogr., *16*, 532–548.

Flagg, C. N., G. Schwartze, E. Gottlieb, and T. Rossby. 1998. Operating an acoustic Doppler current profiler aboard a container vessel. J. Atmos. Oceanic Technol., *15*, 257–271.

Flierl, G. R. 1981. Particle motions in large-amplitude wave fields. Geophys. Astrophys. Fluid Dyn., *18*, 39–74.

Fofonoff, N. P. 1962. Dynamics of ocean currents, *in* The Sea, Vol. 1, Physical Oceanography, M. N. Hill, ed. New York: Wiley-Interscience, 323–395.

Hebert, D., N. Oakey, and B. Ruddick. 1990. Evolution of a Mediterranean salt lens: Scalar properties. J. Phys. Oceanogr., *20*, 1468–1483.

Holte, J., F. Straneo, C. Moffat, R. Weller, and J. T. Farrar. 2013. Structure and surface properties of eddies in the southeast Pacific Ocean. J. Geophys. Res.: Oceans, *118*, 2295–2309. doi: 10.1002/jgrc.20175

Holton, J. R. 1992. An Introduction to Dynamic Meteorology. San Diego, CA: Academic Press, 511 pp.

Hormazabal, S., V. Combes, C. E. Morales, M. A. Correa-Ramirez, E. Di Lorenzo, and S. Nuñez. 2013. Intrathermocline eddies in the coastal transition zone off central Chile (31–41°S). J. Geophys. Res.: Oceans, *118*, 4811–4821. doi: 10.1002/jgrc.20337

Johnson, G. C., and K. E. McTaggart. 2010. Equatorial Pacific 13°C water eddies in the eastern subtropical South Pacific Ocean. J. Phys. Oceanogr., *40*, 226–236.

Kassis, P. 2000. Submesoscale Coherent Vortices in the Deep Brazil Basin. MS thesis. Woods Hole, MA: Massachusetts Institute of Technology and Woods Hole Oceanographic Institution, 66 pp. doi: 10.1575/1912/4189

Luce, D. L., and T. Rossby. 2008. On the size and distribution of rings and coherent vortices in the Sargasso Sea. J. Geophys. Res.: Oceans, *113*, C05011. doi: 10.1029/2007JC004171

McDowell, S. E., and H. T. Rossby. 1978. A mesoscale lens of Mediterranean water off the Bahamas. Science, *202*, 1085–1087.

McWilliams, J. C. 1985. Submesoscale, coherent vortices in the ocean. Rev. Geophys., *23*, 165–182.

Mori, K., K. Uehara, T. Kameda, and S. Kakehi. 2008. Direct measurements of dissipation rate of turbulent kinetic energy of North Pacific subtropical mode water. Geophys. Res. Lett., *35*, L05601. doi: 10.1029/2007GL032867

Moum, J. N., M. C. Gregg, R. C. Lien, and M. E. Carr. 1995. Comparison of turbulence kinetic energy dissipation rate estimates from two ocean microstructure profilers. J. Atmos. Oceanic Technol., *12*, 346–366.

Nof, D. 1981. On the β-induced movement of isolated baroclinic eddies. J. Phys. Oceanogr., *11*, 1662–1672.

Nof, D. 1982. On the movements of deep mesoscale eddies in the North Atlantic. J. Mar. Res., *40*, 57–74.

Nycander, J. 2001. Drift velocity of radiating quasigeostrophic vortices. J. Phys. Oceanogr., *31*, 2178–2185.

Ollitrault, M., and A. C. de Verdiere. 2014. The ocean general circulation near 1000-m depth. J. Phys. Oceanogr., *44*, 384–409.

Prater, M. D., and T. Rossby. 1999. An alternative hypothesis for the origin of the "Mediterranean" salt lens observed off the Bahamas in the fall of 1976. J. Phys. Oceanogr., *29*, 2103–2109.

Richardson, P. L., A. S. Bower, and W. Zenk. 2000. A census of Meddies tracked by floats. Prog. Oceanogr., *45*, 209–250.

Riser, S. C., L. Ren, and A. Wong. 2008. Salinity in Argo. Oceanography, *21*, 56–67.

Rossby, H. T., S. C. Riser, and A. J. Mariano. 1983. The western North Atlantic: A Lagrangian viewpoint, *in* Eddies in Marine Science, A. R. Robinson, ed. Berlin: Springer-Verlag, 66–91.

Rossby, T., C. Flagg, P. Ortner, and C. Hu. 2011. A tale of two eddies: Diagnosing coherent eddies through acoustic remote sensing. J. Geophys. Res.: Oceans, *116*, C12017. doi: 10.1029/2011JC007307

Schultz Tokos, K., and T. Rossby. 1991. Kinematics and dynamics of a Mediterranean salt lens. J. Phys. Oceanogr., *21*, 879–892.

Shoosmith, D. R., P. L. Richardson, A. S. Bower, and H. T. Rossby. 2005. Discrete eddies in the northern North Atlantic as observed by looping RAFOS floats. Deep Sea Res., Part II, *52*, 627–550.

Søiland, H., and T. Rossby. 2013. On the structure of the Lofoten Basin Eddy. J. Geophys. Res.: Oceans, *118*, 4201–4212. doi: 10.1002/jgrc.20301

Talley, L. D., G. L. Pickard, W. J. Emery, and J. H. Swift. 2011. Descriptive Physical Oceanography: An Introduction. Amsterdam: Academic Press, 560 pp.

Received: *18 July 2014*; revised: *24 October 2014*.